Superionic Lithium Intercalation through 2×2 nm^2 Columns in the Crystallographic Shear Phase Nb$_{18}$W$_8$O$_{69}$

Kent J. Griffith[1], Clare P. Grey[1*]

[1]Department of Chemistry, University of Cambridge, CB2 1EW Cambridge, United Kingdom

E-mail: cpg27@cam.ac.uk

Abstract

Nb$_{18}$W$_8$O$_{69}$ (9Nb$_2$O$_5$·8WO$_3$) is the tungsten-rich end-member of the Wadsley–Roth crystallographic shear (*cs*) structures within the Nb$_2$O$_5$–WO$_3$ series. It has the largest block size of any known, stable Wadsley–Roth phase, comprising 5×5 units of corner-shared MO$_6$ octahedra between the shear planes, giving rise to 2 nm × 2 nm blocks. Rapid lithium intercalation is observed in this new candidate battery material and ^{7}Li pulsed field gradient nuclear magnetic resonance spectroscopy – measured in a battery electrode for the first time at room temperature – reveals superionic lithium conductivity with Li diffusivities at 298 K predominantly between 10^{-10} and 10^{-12} m^2·s^{-1}. In addition to its promising rate capability, Nb$_{18}$W$_8$O$_{69}$ adds a piece to the larger picture of our understanding of high-performance Wadsley–Roth complex metal oxides.

Introduction

Safe, durable, high power batteries are necessary for vehicular energy storage in, e.g., passenger vehicles, buses, and warehouse vehicles, where they can assist with acceleration, regenerative braking, and rapid charging. Fast recharge, without accelerated cell degradation, is also important for portable electronics, e-bikes and e-scooters, and frequency-stabilization at the grid scale. Lithium titanate spinel ($Li_4Ti_5O_{12}$) is used as an anode in state-of-the-art, commercial high-rate batteries because it reacts with lithium at 1.55 V vs. Li metal, thus avoiding the propensity for coulombically inefficient and potentially dangerous Li metal deposition on the anode under high charging current densities. However, $Li_4Ti_5O_{12}$ has a low gravimetric and volumetric energy density due to its partial utilization of Ti^{4+} redox centers, cycling between $Li_4Ti_5O_{12}$ and $Li_7Ti_5O_{12}$, and the necessity of nanosizing to enable high-rate operation. The nanoparticle morphology also presents challenges for material scale-up and processing. Alternatives to $Li_4Ti_5O_{12}$ that retain the excellent safety properties but overcome some of the disadvantages could enable wider penetration of high-power battery energy storage.

Niobium-based complex oxides have emerged as promising candidates for high-rate anode materials due to the inherent stability and fast lithium diffusion within some common Nb-oxide structure types as well as the multi-redox capability of niobium (i.e. Nb^{5+} to Nb^{3+}).[1] In this work, we explore $Nb_{18}W_8O_{69}$ ($9Nb_2O_5 \cdot 8WO_3$)[2], the tungsten-rich end member of the xNb$_2$O$_5 \cdot y$WO$_3$ homologous series. This phase represents the last (i.e., highest tungsten content) of the series to adopt a Wadsley–Roth crystallographic shear (*cs*) structure (Figure 1). With increased tungsten content, the niobium tungsten oxides adopt a bronze-like structure, starting with Nb_2WO_8.[3,4] Up to this point, niobium oxide acts a structure-directing agent, in the sense that Nb-rich compounds

form *cs* phases with various block sizes and inter-block connectivities when alloyed with other metal oxides at high temperature. $Nb_{18}W_8O_{69}$ is comprised of the largest $(m \times n)_p$ blocks of octahedra in any known *cs* structure with $(5 \times 5)_1$ blocks. The subscript *p* refers to the connectivity of the $(m \times n)$ blocks of octahedra where individual blocks isolated by tetrahedra correspond to *p* = 1, pairs of blocks correspond to *p* = 2, and chains of blocks without tetrahedra correspond to *p* = ∞. Many *cs* structures (and substituted derivatives) have been investigated including binary H-Nb_2O_5,[5] niobium titanium oxides—$TiNb_2O_7$,[6–8] $Ti_2Nb_{10}O_{29}$,[9–11] $TiNb_{24}O_{62}$,[12,13] and niobium tungsten oxides—$Nb_{12}WO_{33}$,[6,14,15] $Nb_{26}W_4O_{77}$,[16,16] $Nb_{14}W_3O_{44}$,[6,17–19] and $Nb_{16}W_5O_{55}$[1]. These phases vary in block size from (3×3) for $TiNb_2O_7$[20,21] to (4×5) for $Nb_{16}W_5O_{55}$[22].

According to the published phase diagram, $Nb_{18}W_8O_{69}$ is obtained only in a narrow temperature range from ca. 1265–1375 ºC.[23] Like all of the metastable niobium tungsten oxides, it requires a reconstructive phase transition and mobility of highly charged niobium and tungsten cations to convert to the neighboring phases and is thus kinetically stable at room temperature. However, WO_3 sublimes via the gaseous molecules W_3O_9 and W_4O_{12} at these temperatures.[24] There is competition between (i) reaction kinetics and product stability favored at higher temperatures and (ii) reactant stability favored at lower temperatures. Roth and Waring noted in their study of Nb_2O_5–WO_3 phase equilibria that "[T]he binary equilibrium stability regions of this structural group of compounds tend to decrease with increasing W^{6+} content. This phenomenon is probably due to the increasing size of the basic "building block" unit, and therefore to the greater energy needed to maintain long range ordering."[23] $Nb_{18}W_8O_{69}$ presents synthetic challenges but its relation to $Nb_{16}W_5O_{55}$ and its status as the largest known block phase motivate further study as a new electrochemical energy storage material.

Based on lithiation to one lithium per transition metal, the gravimetric capacity of $Nb_{18}W_8O_{69}$ is 164.1 mA·h·g^{-1}. A two electron 'multiredox' process, as observed in other niobium tungsten oxides[1], would lead to 328.2 mA·h·g^{-1}. The high crystal density of 5.37 g·cm^{-3} should lead to electrodes with high volumetric density. Thus, (5 × 5) $Nb_{18}W_8O_{69}$ is interesting as new anode candidate in its own right, but also to help understand the fundamental interplay of block size, composition, and electrochemical properties in the cs phases.

Results and Discussion

$Nb_{18}W_8O_{69}$ was synthesized from niobium pentoxide and tungsten trioxide according to the following heat treatments that were all followed by quenching on a metal plate:

1. heating the ground starting materials in the furnace to 800 ºC at 10 ºC·min^{-1} and holding for 16 h followed by heating to 1280 ºC at 3 ºC·min^{-1} and holding for 2.5 h ($Nb_{18}W_8O_{69}$-I);

2. placing the starting materials into the furnace directly at 1280 ºC for 50 min ($Nb_{18}W_8O_{69}$-II);

3. placing the starting materials into the furnace directly at 1280 ºC for 8 h ($Nb_{18}W_8O_{69}$-III) (Supplementary Figure S1).
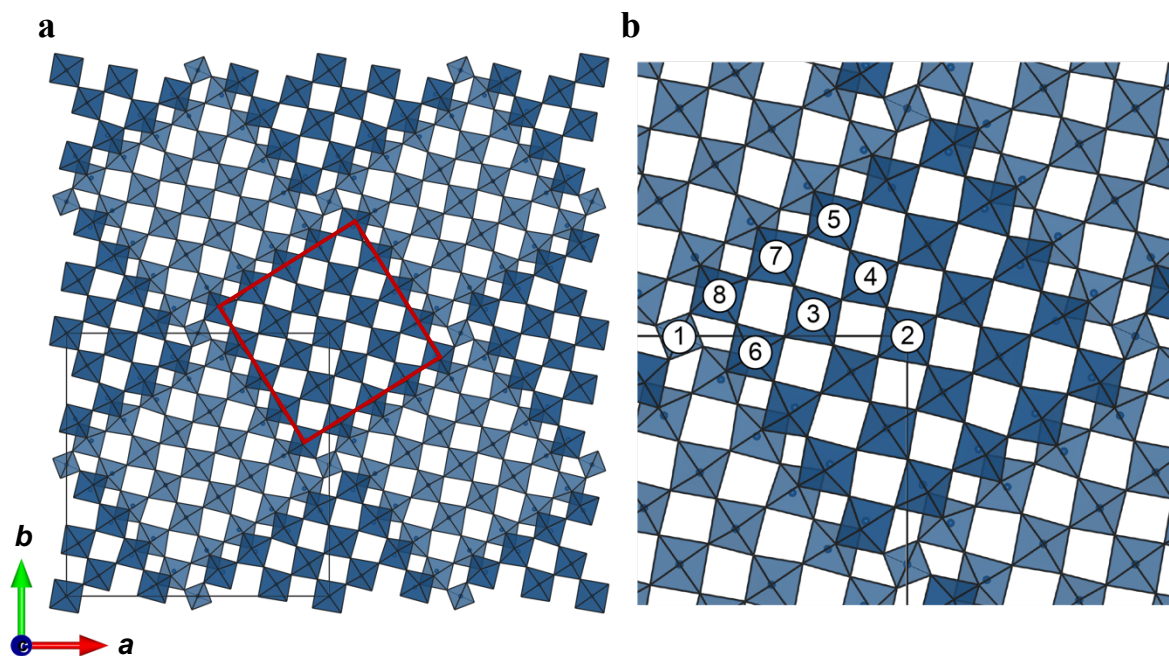
Figure 1 – (a) Crystal structure of $Nb_{18}W_8O_{69}$ comprised of 2 nm × 2 nm blocks formed from columns of ReO_3-like octahedra (outlined red square) in the $I\bar{4}$ space group. The blocks are joined within the same *a-b* plane by tetrahedra, and to blocks offset in the *c*-direction by shear planes. (b) Metal cation sites are labeled following the numbering scheme of Roth and Wadsley,[2] adjusted to accommodate disorder on the tetrahedral site (see Supplementary Table S1 for cross-referenced site labels).

These three conditions were chosen to balance the competition between reactant instability and product stability at high temperature: after 24 h at 1200 ºC, mostly Nb_2WO_8 was found by powder X-ray diffraction (PXRD) but with some shear structure reflections. After 24 h at 1300 ºC, mostly $Nb_{16}W_5O_{55}$ was found by PXRD, which is consistent with the loss of WO_3 via sublimation. The stability range of 1265–1375 ºC for $Nb_{18}W_8O_{69}$ from Roth and Waring[23] was based on an annealing time of 1–3 h in a sealed Pt tube and they always observed $Nb_{16}W_5O_{55}$ as a secondary phase.

The PXRD patterns and electron microscopy images of the three preparations of $Nb_{18}W_8O_{69}$ are nearly identical (Figure 2a, Supplementary Figure 2–3), but with notable differences in some low angle reflections (Figure 2b). All three preparations of $Nb_{18}W_8O_{69}$ exhibit particles with subhedral to euhedral columnar crystal habit and typical dimensions of several μm in diameter by ~10 μm in
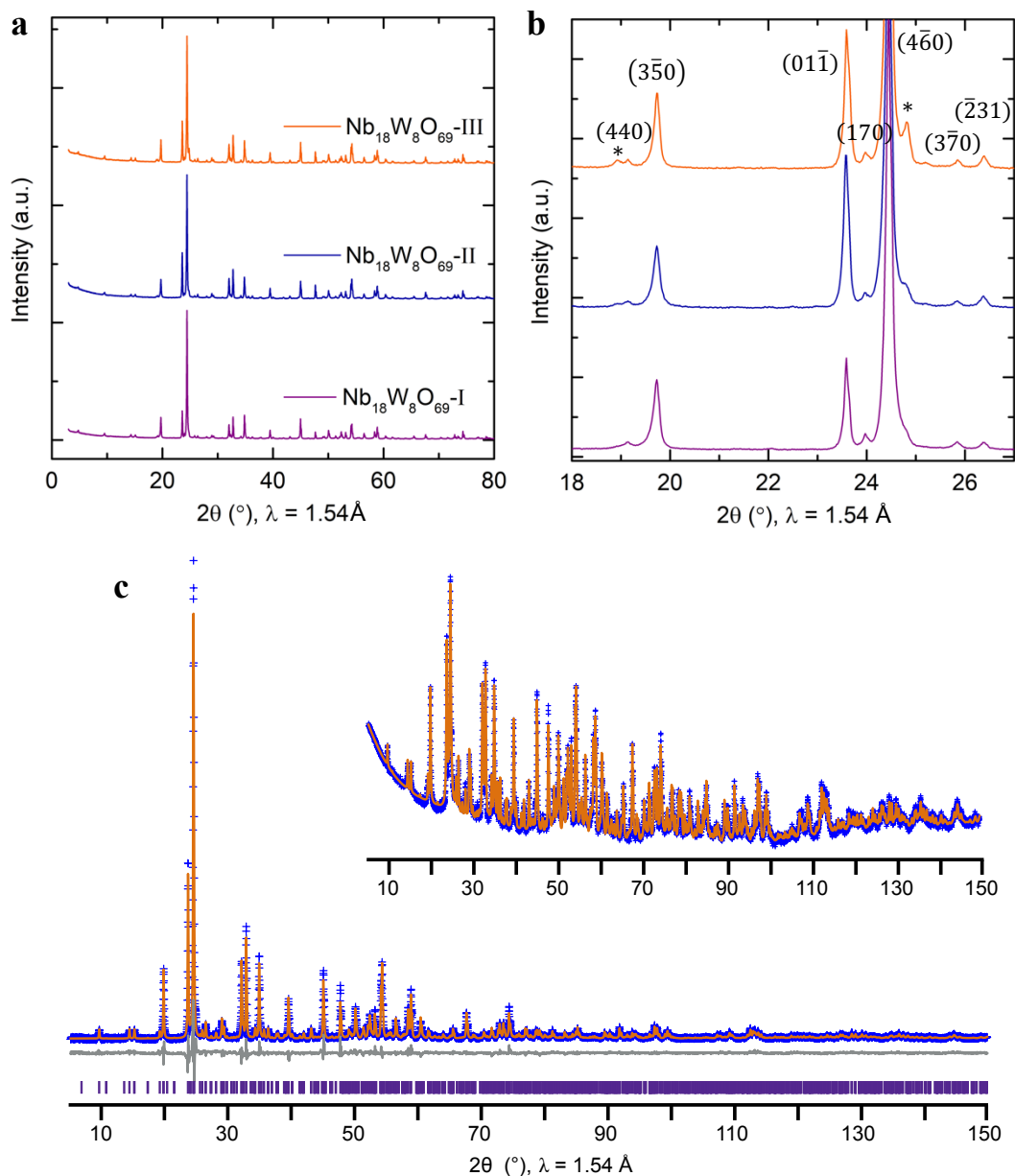

Figure 2 – X-ray diffraction patterns of $Nb_{18}W_8O_{69}$. (a) Full intensity patterns shown from 3–80° 2θ (3–150° 2θ in Supplementary Fig. S2). (b) The region from 18–27° 2θ, with reflections labeled and unindexed peaks marked with asterisks. (c) XRD pattern of $Nb_{18}W_8O_{69}$-II and Rietveld refinement. Data are shown as blue crosses, the fit as an orange curve, the difference as a grey curve, and reflections as vertical purple lines. Inset shows intensity on a log scale.

length (See the SEMs reported in Supplementary Figure S3). Rietveld refinement of the $Nb_{18}W_8O_{69}$ structural model was performed with the X-ray diffraction data from $Nb_{18}W_8O_{69}$-II (Figure 2c). It was immediately apparent that the peak shapes are almost purely Lorentzian. The atomic positions, isotropic atomic displacement parameters, and cation site fractions were refined in GSAS-II[25]. The light atom (i.e. oxygen) parameters are not reliable from the laboratory X-ray data but some tentative conclusions can be drawn regarding niobium and tungsten occupancies (Supplementary Table S1). If Nb^{5+} and W^{6+} were distributed randomly across all cation sites, the expected tungsten partial occupancy would be $4/13 \approx 0.31$. However, the data suggest that tungsten prefers sites $M2$–4 at the center of the blocks while niobium is enriched at $M5$–8 along the crystallographic shear planes. When niobium and tungsten are allowed to mix on the tetrahedral $M1$ site during the Rietveld refinement (Supplementary Table S1), the tungsten occupancy moves away from unity, in contrast to the assumption made by Roth and Wadsley.[2] Cheetham and Allen observed a strong preference for Nb^{5+} at the edges of the $(4 \times 4)_1$ blocks in $Nb_{14}W_3O_{44}$.[26] Koçer *et al.* calculated the cation configurations in $Nb_{14}W_3O_{44}$ and $Nb_{16}W_5O_{55}$ with DFT and Boltzmann statistics.[27] The computational and experimental studies are in agreement; electrostatic repulsion at the edge-shared octahedra along the shear planes leads to preferred cation ordering with the higher charged cation in the block center and the lower charged cation at the block edges.[26,27] A similar trend was observed in the $TiO_2 \cdot Nb_2O_5$ block structures; in this case, though, Nb^{5+} is the higher charged species. Cheetham and Von Dreele[21,28] used neutrons to show that Nb^{5+} prefers the central octahedron in $(3 \times 3)_\infty$ $TiNb_2O_7$—recently confirmed with X-rays for this compound and the Ta analogue[29]. The same phenomenon has been reported in the orthorhombic polymorph of $(3 \times 4)_\infty$ $Ti_2Nb_{10}O_{29}$[21,28] and in $(3 \times 4)_2$ $TiNb_{24}O_{62}$[13].

The low-angle diffraction region is significant in *cs* phases because the long *d*-spacing inter-block arrangement differentiates various *cs* phases with nearly identical short-range structure motifs. The unindexed peaks in Figure 2, that are increasingly pronounced from $Nb_{18}W_8O_{69}$-I to III, do not correspond to expected compounds from the phase diagram such as $Nb_{16}W_5O_{55}$, Nb_2WO_8, $Nb_{14}W_3O_{44}$, $Nb_{12}WO_{33}$, H-Nb_2O_5, or WO_3. Another hypothesis is that these peaks relate to defects in $Nb_{18}W_8O_{69}$. Wadsley defects—coherent intergrowths of different, usually adjacent, cs phases—are characteristic defects in niobium tungsten oxide shear phases. Allpress and Roth studied $Nb_{18}W_8O_{69}$ with electron microscopy and observed both (4 × 5) blocks of octahedra with the nominal composition $Nb_{16}W_5O_{55}$ and (5 × 6) blocks of octahedra with the theoretical composition $Nb_{20}W_{11}O_{83}$.[30] We postulate that the unidentified peaks observed here may be related to extended defect regions within $Nb_{18}W_8O_{69}$.
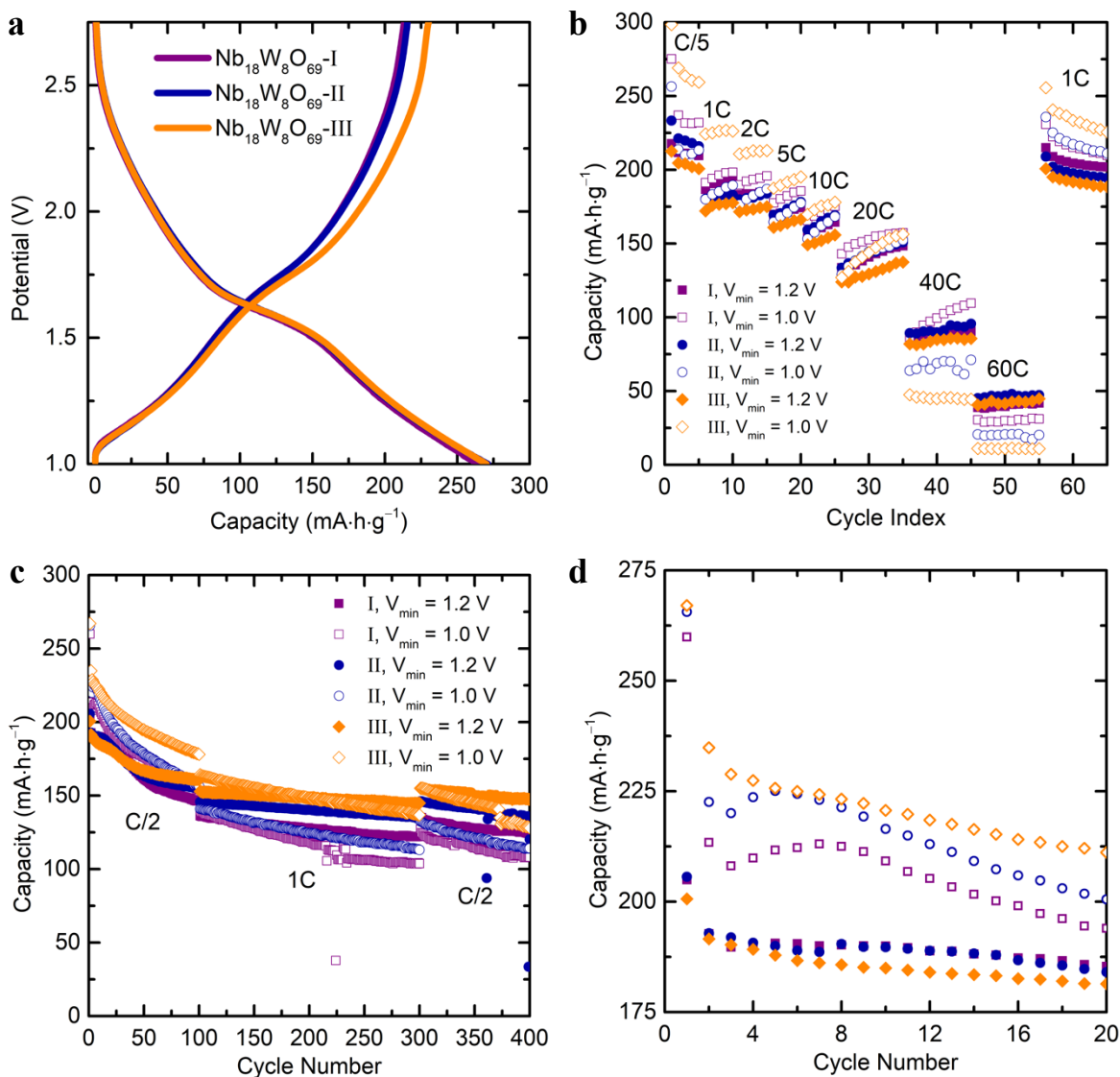
Figure 3 – Electrochemistry of micrometer-scale $Nb_{18}W_8O_{69}$. (a) Discharge and charge profiles at C/2 rate. (b) Rate performance comparison from C/5 to 60C. (c) Cycle performance over 400 total cycles (100 cycles × C/2; 200 cycles × 1C; 100 cycles × C/2). (d) Initial cycle performance from part (c) showing the different first cycle capacity retention and resulting behavior between $Nb_{18}W_8O_{69}$-I –III.

Electrochemical cells were prepared to analyze the lithium intercalation behavior of bulk $Nb_{18}W_8O_{69}$. The C/2 discharge curves of the three versions of $Nb_{18}W_8O_{69}$ were nominally identical (Figure 3a), but the irreversible capacity and cycling performance differed (Figure 3). $Nb_{18}W_8O_{69}$ exhibits similar rate performance to its neighboring *cs* structure $Nb_{16}W_5O_{55}$ up to 20C with similar

particle sizes and electrode preparation.[1] The early cycle capacity retention of $Nb_{18}W_8O_{69}$ is less stable than $Nb_{16}W_5O_{55}$ but on par with reports of other shear structures including H-Nb_2O_5,[31] $Nb_{14}W_3O_{44}$,[19] and $Nb_{12}WO_{33}$.[14,15]. Cells were cycled between 3.0 V and a lower voltage cutoff (V_{min}) of either 1.2 or 1.0 V, with capacity retention being worse for the wider potential window as expected (Figure 3c). The different preparations of $Nb_{18}W_8O_{69}$ all showed the same first cycle capacity when cycled to 1.2 V (205±5 mA·h·g^{-1}) or 1.0 V (265±5 mA·h·g^{-1}) at C/2 but their behaviors deviated thereafter, especially with the lower voltage cut-off (Figure 3c–d).

A characteristic feature of crystallographic shear structures is the (at least) three regions in their electrochemical profiles and corresponding structure evolution: (i) sloping region, (ii) plateau-like region, (iii) sloping region.[32,1,31,27] Examination of the voltage vs. capacity curves and derivative (*dQ/dV*) plots (Figure 4) of $Nb_{18}W_8O_{69}$ reveals a relatively sloped voltage profile. This can be quantified by comparing the full-width half-maximum of the derivative peak for $Nb_{18}W_8O_{69}$ at 250 mV (Figure 4) vs. H-Nb_2O_5 at 40 mV (Figure 4c of ref. [31]). As was previously observed for $TiNb_2O_7$ and $Nb_{16}W_5O_{55}$,[1,33,34] the transition metal cation disorder significantly broadens the electrochemical features relative to that of H-Nb_2O_5. The transition metal cation disorder appears to suppress the proclivity of lithium cation ordering that can lead to phase transitions between low-energy ordered compositions, which can be detrimental for high-rate performance. Another feature that is evident in the *dQ/dV* plots is the asymmetry in lithium insertion vs. extraction (Figure 4b,d). Cycling within a narrower voltage window (Figure 4b), combined with the overpotential, result in a spike at the start of charge at moderate C-rates. On the other hand, the major redox peaks of $Nb_{18}W_8O_{69}$ (1.6–1.7 V) shift minimally up until ≥20C rate even as the initial overpotential increases. Overpotential scales with current density and resistance; the asymmetry shows that this effect is more pronounced on lithium extraction. For clarity we note that, due to the large particle

sizes and small accessible surface areas, we do not ascribe the high-rate performance to capacitive or 'pseudocapacitive' effects. Overall, bulk morphologies of $Nb_{18}W_8O_{69}$ appear to (de)intercalate lithium with rapid kinetics like in the $Nb_{16}W_5O_{55}$ *cs* phase.

To investigate the capacity fade over cycling, voltage and *dQ/dV* profiles were examined over 100 cycles at C/2 rate (Supplementary Figure S4). The onset of lithiation in the 2nd cycle occurs at a higher voltage than the first. This phenomenon was also observed in $Nb_{16}W_5O_{55}$ and attributed to
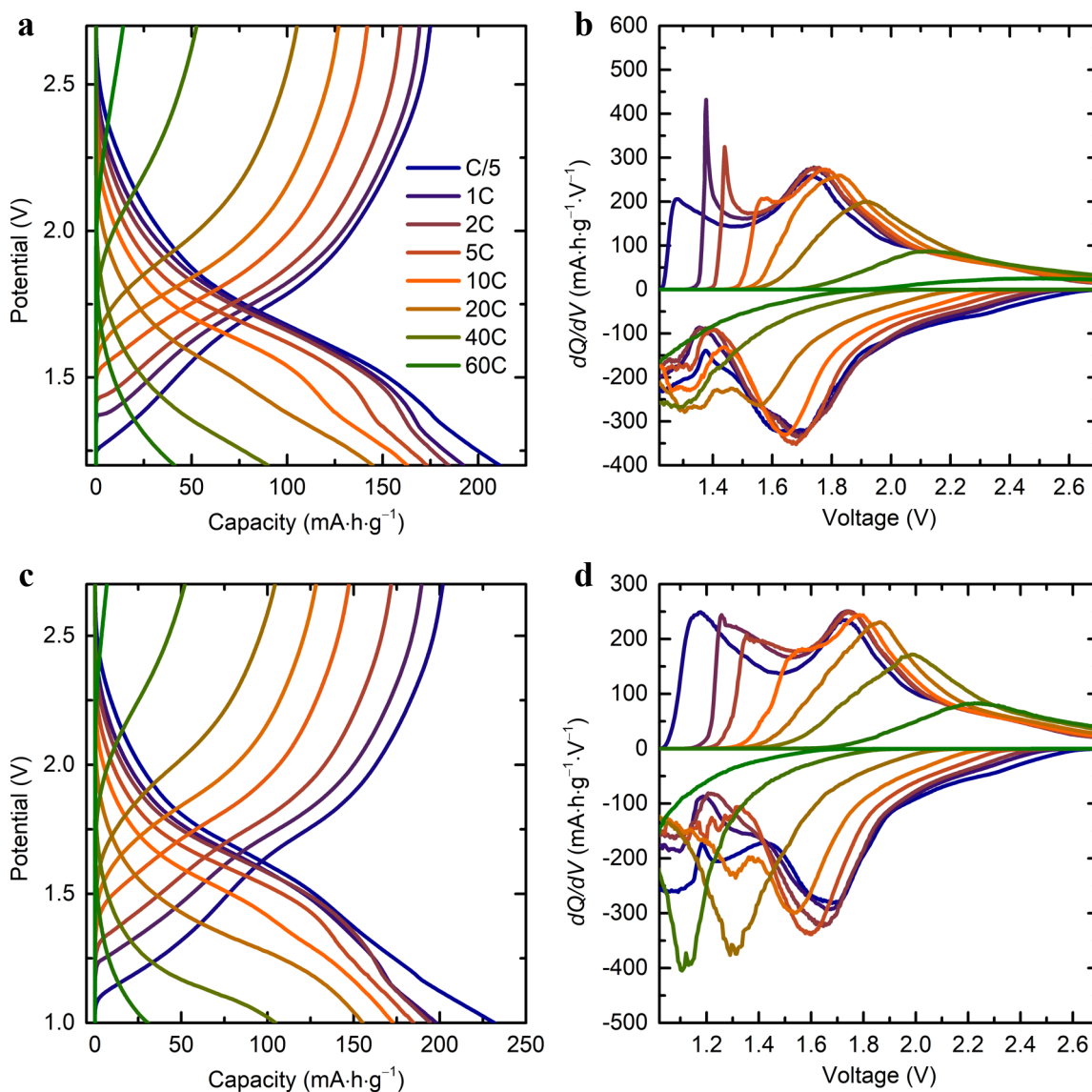

Figure 4 – Electrochemical profiles and *dQ/dV* plots of $Nb_{18}W_8O_{69}$-I. (a,c) Discharge and charge profiles and (b,d) derivative plots as a function of rate from C/5 to 60C. Cycling was performed within the range 3.0 V to (a–b) 1.2 V and (c–d) 1.0 V.

residual lithium in the structure, which increases electronic conductivity by acting as an n-type dopant. Cycling to 1.0 V results in a much larger 1st cycle capacity loss (17.9%, 46.5 mA·h·g^{-1}) than cycling to 1.2 V (6.0%, 12.3 mA·h·g^{-1}). Comparison of the *dQ/dV* curves (Supplementary Figure S4b,d) suggests that cycling to 1.0 V hinders delithiation of the particles; this manifests as a continuous suppression of the first lithium removal peak around 1.19 V and a 200 mV shift to continuously more positive voltages over 100 cycles. For cycling to a lower cutoff voltage of 1.2 V, the oxidative peak shift over 100 cycles is reduced to only 50 mV. In both cases, the second charging peak is unaffected. Notably, the capacity fade in this niobium tungsten oxide differs from the titanium niobium oxide $TiNb_{24}O_{62}$, which shows increasing polarization between its more pronounced reduction and oxidation peaks.[13] The mechanistic difference in degradation between decreasing *dQ/dV* intensity vs. peak shift is consistent with active material loss vs. polarization, respectively.

^{7}Li pulsed field gradient nuclear magnetic resonance (PFG NMR) spectroscopy is commonly applied to liquid and superionic solid electrolytes where lithium diffusion is sufficiently fast and nuclear relaxation is sufficiently slow that it is possible to measure lithium motion over micrometer distances.[35–38] In principle, PFG NMR should be extremely useful for measuring ionic transport properties in mixed ionic–electronic conductors such as battery electrode materials but prior to $Nb_{16}W_5O_{55}$, this had proven impossible due to relatively slow Li$^+$ diffusion and electronic effects.[1] In light of the fast electrochemical intercalation of lithium through the bulk particles of $Nb_{18}W_8O_{69}$, PFG NMR was applied to probe Li diffusion at different states-of-charge and over a range of temperatures.
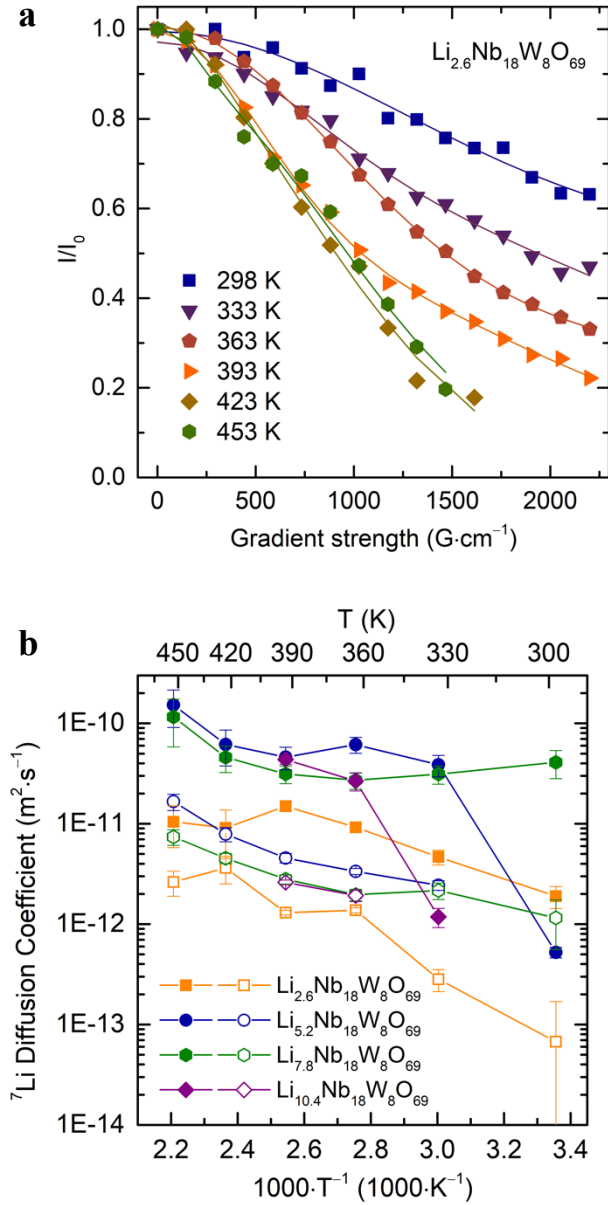
Figure 5 – Li diffusion pulsed field gradient NMR spectroscopy. (a) ^{7}Li signal intensity of $Li_{2.6}Nb_{18}W_8O_{69}$ as a function of magnetic field gradient strength and temperature. Data points are experimental integrals, curves are calculated fits from the Stejskal–Tanner equation. Magnetization decay curves for higher Li contents given in Supplementary Figure S5. (b) Li diffusion coefficients extracted from intensity decay curves via the constrained biexponential Stejskal–Tanner equation with fixed $p = 0.4$, except the lowest temperature point of $Li_{5.2}Nb_{18}W_8O_{69}$ and $Li_{10.4}Nb_{18}W_8O_{69}$ which showed minimal decay (Supplementary Fig. S5) and were fit with a monoexponential curve. Filled and open symbols correspond to $D_{Li,1}$ and $D_{Li,2}$, respectively. Lines in (b) are drawn as guides to the eye. Error bars represent 95% confidence limits.

Lithium diffusion spectra were measured on $Li_xNb_{18}W_8O_{69}$ at $x = 2.6$, 5.2, 7.8, and 10.4, corresponding to 0.1, 0.2, 0.3, and 0.4 Li/TM (Figure 5). Diffusion coefficients were obtained by fitting diffusion-induced magnetization decay curves (e.g. $Li_{2.6}Nb_{18}W_8O_{69}$, Figure 5a) to the Stejskal–Tanner equation[64]:

$$\frac{I}{I_0} = exp\left(-g^2\gamma^2\delta^2\left(\Delta - \frac{\delta}{3}\right)\cdot D_{Li}\right),$$

where I is the observed intensity, I_0 is the intensity without an applied gradient, g is the field gradient, γ is the gyromagnetic ratio ($\gamma_{7Li} = 103.962\times10^6$ rad·s^{-1}·T^{-1}), δ is the effective gradient pulse duration, Δ is the diffusion time, and D_{Li} is the self-diffusion coefficient. Typical δ values ranged from 0.8 ms to 1.2 ms and Δ values ranged from 125–150 ms for $Li_{2.6}Nb_{18}W_8O_{69}$ and 60–80 ms for higher Li concentrations with shorter T_2s. For all lithium concentrations, the experimental data could not be simulated by using a simple monoexponential decay curve. A

biexponential Stejskal–Tanner fit was explored: $\frac{I}{I_0} = p \cdot exp\left(-g^2\gamma^2\delta^2\left(\Delta - \frac{\delta}{3}\right) \cdot D_{Li,1}\right) + (1 -$

$p) \cdot exp\left(-g^2\gamma^2\delta^2\left(\Delta - \frac{\delta}{3}\right) \cdot D_{Li,2}\right)$, where $D_{Li,1}$ and $D_{Li,2}$ are two diffusion coefficients and p is

the fraction of $D_{Li,1}$. This increases the number of variables from one (D_{Li}) to three ($D_{Li,1}$, $D_{Li,2}$, p).

As expected, the value of p is correlated with the extracted diffusion coefficients. Fitting the PFG

diffusion data with a biexponential function increases the uncertainty of these correlated

parameters so the impact of the degrees of freedom (one, two, or three parameters) was evaluated

systematically (Supplementary Figure S7) and 95% confidence intervals were calculated (Figure

5b, Supplementary Figure S7). The best fits to all the data sets were achieved with values of p

fixed between 0.3–0.5 while letting the diffusion coefficients refine (i.e. a constrained

biexponential), with very little difference between goodness-of-fit parameters being obtained in

this range of p (Figure 5, Supplementary Figure S5). Monoexponential, unconstrained

biexponential, and constrained biexponential fits and their implications for the extracted diffusion

coefficients are detailed in the Supporting Information (Supplementary Figures S6 and S7). ^{7}Li

diffusion coefficients from 10^{-13} m^2·s^{-1} to 4×10^{-11} m^2·s^{-1} were observed at room temperature (298

K); high temperature (453 K) diffusion coefficients reached 3×10^{-12} m^2·s^{-1} to 2×10^{-10} m^2·s^{-1}. A

diffusion time of 70 ms at 1×10^{-11} m^2·s^{-1} corresponds to a diffusion length of ~2 μm so these PFG

measurements are probing long-range lithium diffusion on the scale of the particle size.

Non-monoexponential diffusion appears to be a real feature of the niobium tungsten oxide

crystallographic shear phases; the fit to the data with a single-component fit was poor and it is

clear from the decay curves that a biexponential fit is a far better representation of the data

(Supplementary Figure S6). This phenomenon was also observed in Li$_x$Nb$_{16}$W$_5$O$_{55}$[1] whereas the

bronze phase Li$_x$Nb$_{18}$W$_{16}$O$_{93}$ was well-described by a single-component fit. The biexponential

may represent two diffusion processes or it may capture a distribution. The data are insufficient to explore more complex models; however, the current fit does capture the distribution of correlations and rapid transport for all populations of ions – even the slow ones. The structural origin of this complex diffusion may be related to the diversity of tunnels and of sites within the tunnels: there are three classes of tunnels in the material, four per block that border two perpendicular shear planes (i.e., at the corners of the blocks), eight on the edge that border one shear plane, and four in the center of the block that do not border a shear plane. Each tunnel may contain multiple Li local minima.[27] High activation barriers are reported, at least for related phases[34], for hops between blocks, so that transport is essentially one-dimensional along the c axis. Additional distributions in correlation times could also result from differences in the potential energy maps due to tungsten *vs.* niobium substitution in the metal octahedra that form the walls of the tunnels. A characteristic quadrupolar lineshape is observed in the static spectra, even at the highest temperature measured (453K) which reflects the anisotropic environment sampled by the Li ions as they move rapidly down the tunnels (Supplementary Figure S8). At lower temperatures, the signal broadens indicating a slowing down of the motion; furthermore the line shape does not appear to arise from a single environment (i.e., is not consistent with a single second-rank tensor) consistent with the multi-exponential behavior discussed above. The relatively sharp and featureless central transition resonance indicates that exchange between the lithium environments is rapid on the timescale determined by the ^{7}Li chemical shift. A single resonance was also observed in high-resolution magic-angle-spinning ^{6}Li measurements. Non-monoexponential PFG behavior with sharp 1D spectra suggest that lithium ions sample many environments within a block (local hopping) but diffuse down the different tunnels (net long-range diffusion) with a distribution of diffusion coefficients. While a more detailed analysis of the effect of different types of distributions of

correlation times on both the static lineshapes, and on the PFG measurements, will be a subject of future work, the analysis presented here clearly indicates Li diffusivities of between 10^{-10} and 10^{-12} $m^2 \cdot s^{-1}$.

To the best of our knowledge, these are the first room temperature ^7Li PFG NMR diffusion measurements on battery electrodes. The room-temperature lithium self-diffusion coefficients in $Li_xNb_{18}W_8O_{69}$ are orders-of-magnitude faster than that of common battery electrode materials[1] and are more comparable to the fastest superionic lithium sulfide electrolytes ($LiTi_2(PS_4)_3$ at 1.2×10^{-11} $m^2 \cdot s^{-1}$; $Li_{11}Si_2PS_{12}$ at 3.5×10^{-12} $m^2 \cdot s^{-1}$).[39,37] For comparison, room-temperature Li^+ diffusion in 1.0 M PF_6 in organic carbonate electrolytes is 8.3–25×10^{-11} $m^2 \cdot s^{-1}$ and Ag^+ diffusion in the fastest known superionic conducting solid—$AgRb_4I_5$—is 2×10^{-10} $m^2 \cdot s^{-1}$.[38,40] At higher lithium concentrations, T_1 and T_2 relaxation were too fast to allow sufficient diffusion distances or the application of a sufficient gradient pulse, respectively. We note that elevated temperatures were also required to overcome rapid T_2 relaxation in our previous study demonstrating ^7Li PFG NMR diffusion measurements on $Li_xNb_{16}W_5O_{55}$ at $x = 6.3$ and 8.4. It is expected that $Nb_{16}W_5O_{55}$ and $Nb_{18}W_8O_{69}$ become metallic at higher lithium contents and the nuclear relaxation is enhanced by conduction electrons.[27]

The transition from wide band gap insulator to conductor is supported by optical measurements. Prior to lithiation, $Nb_{18}W_8O_{69}$ is off-white (light yellow-green) with an optical bandgap of 2.84 eV (Supplementary Figure S9). Upon lithium insertion, the color becomes dark blue. Experimental and theoretical work on related *cs* phases suggests that lithiation reduces d^0 Nb^{5+} and W^{6+},[1] n-doping the structure into the conduction band and causing an increase in electronic

conductivity,[27,34,41] which motivates detailed future work to understand subtle differences between compositionally and structurally similar *cs* compounds.
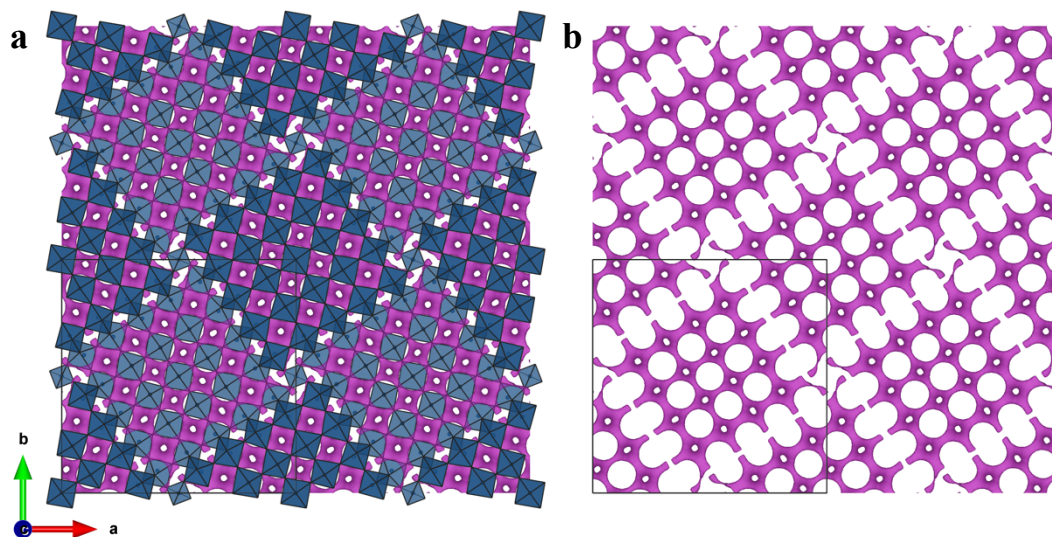

Figure 6 – Lithium bond valence energy landscape map of $Nb_{18}W_8O_{69}$. (a) BVEL map showing the 5 × 5 crystallographic shear blocks of octahedra (blue) and probable lithium positions. (b) Probable lithium diffusion pathways shown without the structure model for clarity.

The tunnels within the blocks of Wadsley–Roth crystallographic shear structures enable lithium transport and the 5 × 5 blocks of octaheda in $Nb_{18}W_8O_{69}$ are the largest that have been synthesized as an isolated phase. These 2 nm × 2 nm blocks give rise to sixteen parallel lithium tunnels with twelve that are adjacent to shear planes (i.e. 'edge' tunnels) and four that are central and ReO_3-like (i.e. 'central' tunnels). Bond valence sum maps (Figure 6) and calculations on related systems indicate that lithium moves through both types of tunnel.[42,34] It is not known how the dynamics differ at central vs. edge tunnels; this is an interesting question requiring computational insights, though it is non-trivial as diffusion barriers are highly sensitive to the specific transition metal cation ordering in Wadsley–Roth $TiNb_2O_7$.[34] Regardless, the large blocks offer a maximal number of tunnels and rapid Li^+ conductivity. That the rate performance of $Nb_{18}W_8O_{69}$ is not higher than

$Nb_{16}W_5O_{55}$ may reflect other factors, besides bulk Li^+ diffusion, that impact charge and discharge rate including microstructural and electronic effects. For example, little is yet known in $Nb_{18}W_8O_{69}$ or other *cs* phases regarding the extent or impact of Wadsley defects nor the nature or impact of crystal facets or surface chemistry on the battery performance. Furthermore, systematic studies are needed to correlate electrochemical properties with particle size and morphology in the Wadsley–Roth phases. A related consequence of the large block size in $Nb_{18}W_8O_{69}$ is that it has the lowest density of *cs* planes in the Wadsley–Roth structures. The shear planes are thought to provide stability by decreasing the structural degrees of freedom and preventing the tilts and distortions common to unstabilized ReO_3 and WO_3 upon lithiation.[43–46] An appropriate balance between conducting tunnels and stabilizing shear planes is thus desired for high-rate battery performance but the optimal shear structure is not established. From the small but growing body of literature on Wadsley–Roth phases, there is no clear trend between long-term stability and shear plane density or shear plane arrangement, though many variables stand between the idealized atomic structure and battery performance. In addition to device fabrication and microstructural considerations, an unavoidable complication is that the variation in the blocks is accompanied by changes in composition. Though Wadsley defects are generally expected, a further challenge in understanding this family is that the exact type, concentration, arrangement, and role of defects is not well-known nor easy to determine. Future work could consider other subtle fundamental aspects of the interplay between synthesis–structure–defects–electrochemistry, the relationship between lithium content and reversibility, and practical strategies to increase the cycle stability of superionic $Nb_{18}W_8O_{69}$ and enable its use in ultrafast charging and high power energy storage.

Conclusion

$Nb_{18}W_8O_{69}$, with a crystallographic shear structure, hosts superionic lithium ion conductivity that leads to battery rate performance on par with recently reported members of the Nb_2O_5–WO_3 phase diagram including shear phase $Nb_{16}W_5O_{55}$ and bronze-like phase $Nb_{18}W_{16}O_{93}$. PFG NMR was able to directly capture room temperature lithium diffusion of up to 10^{-11} $m^2 \cdot s^{-1}$ for the majority ^7Li signal contribution in this mixed ionic–electronic conductor. The 5×5 blocks of $(Nb/W)O_6$ octahedra in $Nb_{18}W_8O_{69}$ provide 16 parallel tunnels for long-range lithium diffusion, which may explain its high Li^+ diffusion. $Nb_{18}W_8O_{69}$ is a metastable member of the Nb_2O_5–WO_3 phase diagram and variation in synthetic procedures lead to subtly different diffraction patterns and capacity retention. Understanding the nature of the defect chemistry and optimizing the synthesis accordingly could lead to improved electrochemical cycling performance in this and related Wadsley–Roth phases.

Experimental

$Nb_{18}W_8O_{69}$ was prepared from Nb_2O_5 (Sigma, 99.99%, 9:1 T-phase:H-phase, white) and WO_3 (Alfa, 99.8%, γ-phase, light green) ground together with an agate mortar and pestle, uniaxially pressed into a free-standing pellet, and annealed in a covered Pt crucible via three different heating procedures described in the main text. X-ray diffraction was measured with a Panalytical diffractometer equipped with a Cu K_α source in Bragg–Brentano geometry. Data were collected at ambient temperature at $0.83° \cdot min^{-1}$ from 3–150° 2θ whilst the sample stage was continuously rotated to improve powder averaging. Rietveld refinement was performed with GSAS-II,[25] structural representations were drawn in VESTA,[47] and bond valence sum maps were calculated with 3DBVSMAPPER[48]. SEM images were recorded with a MIRA3 instrument (TESCAN) at 3.0

kV accelerating voltage and secondary electron detection. Diffuse reflectance spectra were measured with a Varian UV–visible spectrophotometer from 200–800 nm. Three spectra were recorded, background subtracted, and averaged for each sample.

Electrochemical measurements were made on coin cells constructed with a $Nb_{18}W_8O_{69}$:carbon:binder working electrode (80:10:10 mass ratio) paired against a Li metal counter electrode (LTS Research, 99.95%) and separated by a glass fiber disk (Whatman). The metal oxide was ground in an agate mortar and pestle with SuperP carbon (Timcal) before the mixture was added to a solution of poly(vinylidene difluoride) (PVDF, Kynar) dissolved in N-methyl pyrrolidone (NMP, Sigma-Aldrich, anhydrous, 99.5%). SuperP carbon is a nanoparticulate powder and NMP is a hazardous organic solvent, so appropriate nanoparticle cabinets and fume hoods should be used. 1.0 M $LiPF_6$ dissolved in 1:1 v/v ethylene carbonate/dimethyl carbonate (EC/DMC, Sigma-Aldrich, battery grade, as received) was used as the electrolyte with no additives. Devices were assembled in an argon glovebox with <1 ppm O_2 and <1 ppm H_2O. Electrode active materials mass loadings were 2.0 ± 0.2 mg·cm^{-2}. Electrochemistry was performed in a temperature-controlled room at 293 K with a Biologic galvanostat/potentiostat running EC-Lab software. Accessible capacity and, therefore, C-rate are not well-defined in the Wadsley–Roth phases due to the sloping voltage profiles that lead to a strong dependence of capacity on the voltage window; multielectron redox of both Nb^{5+} to Nb^{3+} and W^{6+} to W^{4+} are known.[1] In these phases, we believe the most convenient method is to defined C-rate relative to one electron transfer per transition metal: for $Nb_{18}W_8O_{69}$ (to $Li_{26}Nb_{18}W_8O_{69}$): 1C = 164.1 mA·g^{-1}, 20C = 3282 mA·g^{-1}.

PFG NMR ^{7}Li diffusion measurements were carried out as described in detail in reference [1]. Lithium niobium tungsten oxide samples were prepared by electrochemically lithiating 210±20 mg pellets of $Nb_{18}W_8O_{69}$ over the course of 60–100 h in coin cells following the procedures previously described. After lithiation, the cells were brought into the inert atmosphere of the glovebox where the electrodes were extracted, washed with DMC (3 × 2 mL), dried under the vacuum of the prechamber, ground in an agate mortar and pestle, and packed into 4.0 mm zirconia rotors that were then sealed into J. Young NMR tubes. Signal-to-noise (S/N) is particularly important for PFG NMR because it measures signal decay so the initial ($g = 0$) S/N ratios are given for all compositions and temperatures (Supplementary Table S2). All diffusion measurements were performed on $Nb_{18}W_8O_{69}$-I due to the similarity of the electrochemical rate performance of the three samples and to the time-consuming nature of variable temperature and variable composition PFG NMR experiments on partially discharged battery electrode materials.

Associated Content

Supporting Information PDF containing synthesis heating profiles, SEM images, diffraction patterns, electrochemical data, PFG NMR decay curves and fitting models, 1D NMR spectra, diffuse reflectance spectra, crystal structure data, and quantification of the attained signals for each PFG NMR measurement.

Author Information

Corresponding Author

Email: cpg27@cam.ac.uk

Notes

Acknowledgements

References

(1) Griffith, K. J.; Wiaderek, K. M.; Cibin, G.; Marbella, L. E.; Grey, C. P. Niobium Tungsten Oxides for High-Rate Lithium-Ion Energy Storage. *Nature* **2018**, *559* (7715), 556–563. https://doi.org/10.1038/s41586-018-0347-0.

(2) Roth, R. S.; Wadsley, A. D. Multiple Phase Formation in the Binary System Nb_2O_5–WO_3. III. The Structures of the Tetragonal Phases $W_3Nb_{14}O_{44}$ and $W_8Nb_{18}O_{69}$. *Acta Crystallogr.* **1965**, *19* (1), 38–42. https://doi.org/10.1107/S0365110X65002736.

(3) Lundberg, M.; Lundeland, M.; Marøy, K.; Tricker, M. J.; Svensson, S. The Crystal Structure of Nb_2WO_8. *Acta Chem. Scand.* **1972**, *26*, 2932–2940. https://doi.org/10.3891/acta.chem.scand.26-2932.

(4) Hyde, B. G.; O'Keeffe, M. Relations between the DO_9 (ReO_3) Structure Type and Some "bronze" and "Tunnel" Structures. *Acta Crystallogr. A* **1973**, *29* (3), 243–248. https://doi.org/10.1107/S056773947300063X.

(5) Kumagai, N.; Koishikawa, Y.; Komaba, S.; Koshiba, N. Thermodynamics and Kinetics of Lithium Intercalation into Nb_2O_5 Electrodes for a 2 V Rechargeable Lithium Battery. *J. Electrochem. Soc.* **1999**, *146* (9), 3203–3210. https://doi.org/10.1149/1.1392455.

(6) Cava, R. J.; Murphy, D. W.; Zahurak, S. M. Lithium Insertion in Wadsley–Roth Phases Based on Niobium Oxide. *J. Electrochem. Soc.* **1983**, *130* (12), 2345–2351. https://doi.org/10.1149/1.2119583.

(7) Han, J.-T.; Huang, Y.-H.; Goodenough, J. B. New Anode Framework for Rechargeable Lithium Batteries. *Chem. Mater.* **2011**, *23* (8), 2027–2029. https://doi.org/10.1021/cm200441h.

(8) Catti, M.; Pinus, I.; Knight, K. Lithium Insertion Properties of $Li_xTiNb_2O_7$ Investigated by Neutron Diffraction and First-Principles Modelling. *J. Solid State Chem.* **2015**, *229*, 19–25. https://doi.org/10.1016/j.jssc.2015.05.011.

(9) Wu, X.; Miao, J.; Han, W.; Hu, Y.-S.; Chen, D.; Lee, J.-S.; Kim, J.; Chen, L. Investigation on $Ti_2Nb_{10}O_{29}$ Anode Material for Lithium-Ion Batteries. *Electrochem. Commun.* **2012**, *25*, 39–42. https://doi.org/10.1016/j.elecom.2012.09.015.

(10) Cheng, Q.; Liang, J.; Zhu, Y.; Si, L.; Guo, C.; Qian, Y. Bulk $Ti_2Nb_{10}O_{29}$ as Long-Life and High-Power Li-Ion Battery Anodes. *J. Mater. Chem. A* **2014**, *2* (41), 17258–17262. https://doi.org/10.1039/C4TA04184D.

(11) Liu, X.; Wang, H.; Zhang, S.; Liu, G.; Xie, H.; Ma, J. Design of Well-Defined Porous $Ti_2Nb_{10}O_{29}$/C Microspheres Assembled from Nanoparticles as Anode Materials for High-Rate Lithium Ion Batteries. *Electrochimica Acta* **2018**, *292*, 759–768. https://doi.org/10.1016/j.electacta.2018.09.133.

(12) Yang, C.; Deng, S.; Lin, C.; Lin, S.; Chen, Y.; Li, J.; Wu, H. Porous $TiNb_{24}O_{62}$ Microspheres as High-Performance Anode Materials for Lithium-Ion Batteries of Electric Vehicles. *Nanoscale* **2016**, *8* (44), 18792–18799. https://doi.org/10.1039/C6NR04992C.

(13) Griffith, K. J.; Senyshyn, A.; Grey, C. P. Structural Stability from Crystallographic Shear in TiO_2–Nb_2O_5 Phases: Cation Ordering and Lithiation Behavior of $TiNb_{24}O_{62}$. *Inorg. Chem.* **2017**, *56* (7), 4002–4010. https://doi.org/10.1021/acs.inorgchem.6b03154.

(14) Saritha, D.; Pralong, V.; Varadaraju, U. V.; Raveau, B. Electrochemical Li Insertion Studies on $WNb_{12}O_{33}$—A Shear ReO_3 Type Structure. *J. Solid State Chem.* **2010**, *183* (5), 988–993. https://doi.org/10.1016/j.jssc.2010.03.003.

(15) Yan, L.; Lan, H.; Yu, H.; Qian, S.; Cheng, X.; Long, N.; Zhang, R.; Shui, M.; Shu, J. Electrospun $WNb_{12}O_{33}$ Nanowires: Superior Lithium Storage Capability and Their Working Mechanism. *J. Mater. Chem. A* **2017**, *5* (19), 8972–8980. https://doi.org/10.1039/C7TA01784G.

(16) Fuentes, A. F.; de la Cruz, A. M.; Torres-Martínez, L. M. A Study of Lithium Insertion in $W_4Nb_{26}O_{77}$: Synthesis and Characterization of New Phases. *Solid State Ion.* **1996**, *92* (1–2), 103–111. https://doi.org/10.1016/S0167-2738(96)00374-8.

(17) Fuentes, A. F.; Martinez De La Cruz, A.; Torres-Martinez, L. M. A Comparative Study of Lithium and Sodium Insertion in Two Block Structure Type Phases, $W_3Nb_{14}O_{44}$ and $W_4Nb_{26}O_{77}$. In *Symposium R – Solid State Chemistry of Inorganic Materials*; MRS Online Proceedings Library; 1996; Vol. 453, p 659. https://doi.org/10.1557/PROC-453-659.

(18) Fuentes, A. F.; Garza, E. B.; de la Cruz, A. M.; Torres-Martínez, L. M. Lithium and Sodium Insertion in $W_3Nb_{14}O_{44}$, a Block Structure Type Phase. *Solid State Ion.* **1997**, *93* (3–4), 245–253. https://doi.org/10.1016/S0167-2738(96)00537-1.

(19) Yan, L.; Shu, J.; Cheng, X.; Zhu, H.; Yu, H.; Zhang, C.; Zheng, Y.; Xie, Y.; Guo, Z. $W_3Nb_{14}O_{44}$ Nanowires: Ultrastable Lithium Storage Anode Materials for Advanced Rechargeable Batteries. *Energy Storage Mater.* **2019**, *16*, 535–544. https://doi.org/10.1016/j.ensm.2018.09.008.

(20) Wadsley, A. D. Mixed Oxides of Titanium and Niobium. I. *Acta Crystallogr.* **1961**, *14* (6), 660–664. https://doi.org/10.1107/S0365110X61001996.

(21) Dreele, R. B. V.; Cheetham, A. K. The Structures of Some Titanium-Niobium Oxides by Powder Neutron Diffraction. *Proc. R. Soc. Lond. Math. Phys. Eng. Sci.* **1974**, *338* (1614), 311–326. https://doi.org/10.1098/rspa.1974.0088.

(22) Roth, R. S.; Wadsley, A. D. Multiple Phase Formation in the Binary System Nb_2O_5–WO_3. II. The Structure of the Monoclinic Phases $WNb_{12}O_{33}$ and $W_5Nb_{16}O_{55}$. *Acta Crystallogr.* **1965**, *19* (1), 32–38. https://doi.org/10.1107/S0365110X65002724.

(23) Roth, R. S.; Waring, J. L. Phase Equilibria as Related to Crystal Structure in the System Niobium Pentoxide-Tungsten Trioxide. *J. Res. Natl. Bur. Stand.* **1966**, *70A* (4), 281–303. https://nvlpubs.nist.gov/nistpubs/jres/70A/jresv70An4p281_A1b.pdf.

(24) Berkowitz, J.; Chupka, W. A.; Inghram, M. G. Polymeric Gaseous Species in the Sublimation of Tungsten Trioxide. *J. Chem. Phys.* **1957**, *27* (1), 85–86. https://doi.org/10.1063/1.1743722.

(25) Toby, B. H.; Von Dreele, R. B. GSAS-II: The Genesis of a Modern Open-Source All Purpose Crystallography Software Package. *J. Appl. Crystallogr.* **2013**, *46* (2), 544–549. https://doi.org/10.1107/S0021889813003531.

(26) Cheetham, A. K.; Allen, N. C. Cation Distribution in the Complex Oxide, $W_3Nb_{14}O_{44}$; a Time-of-Flight Neutron Diffraction Study. *J. Chem. Soc. Chem. Commun.* **1983**, No. 22, 1370. https://doi.org/10.1039/c39830001370.

(27) Koçer, C. P.; Griffith, K. J.; Grey, C. P.; Morris, A. J. Cation Disorder and Lithium Insertion Mechanism of Wadsley–Roth Crystallographic Shear Phases from First Principles. *J. Am. Chem. Soc.* **2019**, *141* (38), 15121–15134. https://doi.org/10.1021/jacs.9b06316.

(28) Cheetham, A. K.; Dreele, V.; B, R. Cation Distributions in Niobium Oxide Block Structures. *Nature* **1973**, *244* (139), 139–140. https://doi.org/10.1038/10.1038/physci244139a0.

(29) Perfler, L.; Kahlenberg, V.; Wikete, C.; Schmidmair, D.; Tribus, M.; Kaindl, R. Nanoindentation, High-Temperature Behavior, and Crystallographic/Spectroscopic Characterization of the High-Refractive-Index Materials $TiTa_2O_7$ and $TiNb_2O_7$. *Inorg. Chem.* **2015**, *54* (14), 6836–6848. https://doi.org/10.1021/acs.inorgchem.5b00733.

(30) Allpress, J. G.; Roth, R. S. The Effect of Annealing on the Concentration of Wadsley Defects in the Nb_2O_5–WO_3 System. *J. Solid State Chem.* **1971**, *3* (2), 209–216. https://doi.org/10.1016/0022-4596(71)90030-2.

(31) Griffith, K. J.; Forse, A. C.; Griffin, J. M.; Grey, C. P. High-Rate Intercalation without Nanostructuring in Metastable Nb_2O_5 Bronze Phases. *J. Am. Chem. Soc.* **2016**, *138* (28), 8888–8899. https://doi.org/10.1021/jacs.6b04345.

(32) Patoux, S.; Dolle, M.; Rousse, G.; Masquelier, C. A Reversible Lithium Intercalation Process in an ReO3 -Type Structure PNb_9O_{25}. *J. Electrochem. Soc.* **2002**, *149* (4), A391–A400. https://doi.org/10.1149/1.1455647.

(33) Lu, X.; Jian, Z.; Fang, Z.; Gu, L.; Hu, Y.-S.; Chen, W.; Wang, Z.; Chen, L. Atomic-Scale Investigation on Lithium Storage Mechanism in $TiNb_2O_7$. *Energy Environ. Sci.* **2011**, *4* (8), 2638–2644. https://doi.org/10.1039/C0EE00808G.

(34) Griffith, K. J.; Seymour, I. D.; Hope, M. A.; Butala, M. M.; Lamontagne, L. K.; Preefer, M. B.; Koçer, C. P.; Henkelman, G.; Morris, A. J.; Cliffe, M. J.; Dutton, S. E.; Grey, C. P. Ionic and Electronic Conduction in $TiNb_2O_7$. *J. Am. Chem. Soc.* **2019**, *141*, 16706−16725. https://doi.org/10.1021/jacs.9b06669.

(35) Wang, Z.; Gobet, M.; Sarou-Kanian, V.; Massiot, D.; Bessada, C.; Deschamps, M. Lithium Diffusion in Lithium Nitride by Pulsed-Field Gradient NMR. *Phys. Chem. Chem. Phys.* **2012**, *14* (39), 13535–13538. https://doi.org/10.1039/C2CP42391J.

(36) Kuhn, A.; Duppel, V.; V. Lotsch, B. Tetragonal $Li_{10}GeP_2S_{12}$ and Li_7GePS_8 – Exploring the Li Ion Dynamics in LGPS Li Electrolytes. *Energy Environ. Sci.* **2013**, *6* (12), 3548–3552. https://doi.org/10.1039/C3EE41728J.

(37) Kuhn, A.; Gerbig, O.; Zhu, C.; Falkenberg, F.; Maier, J.; Lotsch, B. V. A New Ultrafast Superionic Li-Conductor: Ion Dynamics in $Li_{11}Si_2PS_{12}$ and Comparison with Other Tetragonal LGPS-Type Electrolytes. *Phys. Chem. Chem. Phys.* **2014**, *16* (28), 14669–14674. https://doi.org/10.1039/C4CP02046D.

(38) Hayamizu, K. Temperature Dependence of Self-Diffusion Coefficients of Ions and Solvents in Ethylene Carbonate, Propylene Carbonate, and Diethyl Carbonate Single Solutions and Ethylene Carbonate + Diethyl Carbonate Binary Solutions of $LiPF_6$ Studied by NMR. *J. Chem. Eng. Data* **2012**, *57* (7), 2012–2017. https://doi.org/10.1021/je3003089.

(39) Di Stefano, D.; Miglio, A.; Robeyns, K.; Filinchuk, Y.; Lechartier, M.; Senyshyn, A.; Ishida, H.; Spannenberger, S.; Prutsch, D.; Lunghammer, S.; Rettenwander, D.; Wilkening, M.; Roling, B.; Kato, Y.; Hautier, G. Superionic Diffusion through Frustrated Energy Landscape. *Chem* **2019**, *5* (9), 2450–2460. https://doi.org/10.1016/j.chempr.2019.07.001.

(40) Looser, H.; Mali, M.; Roos, J.; Brinkmann, D. Ag Diffusion Constant in $RbAg_4I_5$ and KAg_4I_5 Determined by Pulsed Magnetic Gradient NMR. *Solid State Ion.* **1983**, *9–10*, 1237–1240. https://doi.org/10.1016/0167-2738(83)90158-3.

(41) Koçer, C. P.; Griffith, K. J.; Grey, C. P.; Morris, A. J. First-Principles Study of Localized and Delocalized Electronic States in Crystallographic Shear Phases of Niobium Oxide. *Phys. Rev. B* **2019**, *99* (7), 075151. https://doi.org/10.1103/PhysRevB.99.075151.

(42) P. Parras, J.; R. Genreith-Schriever, A.; Zhang, H.; T. Elm, M.; Norby, T.; Souza, R. A. D. Is ReO_3 a Mixed Ionic–Electronic Conductor? A DFT Study of Defect Formation and Migration in a $B^{VI}O_3$ Perovskite-Type Oxide. *Phys. Chem. Chem. Phys.* **2018**, *20* (12), 8008–8015. https://doi.org/10.1039/C7CP08214B.

(43) Cava, R. J.; Santoro, A.; Murphy, D. W.; Zahurak, S.; Roth, R. S. Structural Aspects of Lithium Insertion in Oxides: Li_xReO_3 and $Li_2FeV_3O_8$. *Solid State Ion.* **1981**, *5*, 323–326. https://doi.org/10.1016/0167-2738(81)90258-7.

(44) Cava, R. J.; Santoro, A.; Murphy, D. W.; Zahurak, S.; Roth, R. S. The Structures of Lithium-Inserted Metal Oxides: $LiReO_3$ and Li_2ReO_3. *J. Solid State Chem.* **1982**, *42* (3), 251–262. https://doi.org/10.1016/0022-4596(82)90004-4.

(45) Cava, R. J.; Santoro, A.; Murphy, D. W.; Zahurak, S. M.; Roth, R. S. The Structures of the Lithium Inserted Metal Oxides $Li_{0.2}ReO_3$ and $Li_{0.36}WO_3$. *J. Solid State Chem.* **1983**, *50* (1), 121–128. https://doi.org/10.1016/0022-4596(83)90239-6.

(46) Qi, K.; Wei, J.; Sun, M.; Huang, Q.; Li, X.; Xu, Z.; Wang, W.; Bai, X. Real-Time Observation of Deep Lithiation of Tungsten Oxide Nanowires by In Situ Electron Microscopy. *Angew. Chem. Int. Ed.* **2015**, *54* (50), 15222–15225. https://doi.org/10.1002/anie.201508112.

(47) Momma, K.; Izumi, F. VESTA 3 for Three-Dimensional Visualization of Crystal, Volumetric and Morphology Data. *J. Appl. Crystallogr.* **2011**, *44* (6), 1272–1276. https://doi.org/10.1107/S0021889811038970.

(48) Sale, M.; Avdeev, M. 3DBVSMAPPER: A Program for Automatically Generating Bond-Valence Sum Landscapes. *J. Appl. Crystallogr.* **2012**, *45* (5), 1054–1056. https://doi.org/10.1107/S0021889812032906.

For table of contents only

$Li_xNb_{18}W_8O_{69}$

Li-ion battery anode

^{7}Li Pulsed Field Gradient NMR

I/I_0

- ■ 298 K
- ▼ 333 K
- ⬠ 363 K
- ▶ 393 K

Gradient strength